Assembly of Core/Shell Nanospheres of Amorphous Hemin/Acetone-Derived Carbonized Polymer with Graphene Nanosheets for Room-Temperature NO Sensing

Wang, Jianqiang; Gao, Yixun; Chen, Fengjia; Zhang, Lulu; Li, Hao; De Rooij, Nicolaas Frans; Umar, Ahmad; Lee, Yi Kuen; French, Paddy J.; More Authors

DOI
10.1021/acsami.2c16769

Publication date
2022

Document Version
Final published version

Published in
ACS Applied Materials and Interfaces

ACS APPLIED MATERIALS & INTERFACES

www.acsami.org

Research Article

Assembly of Core/Shell Nanospheres of Amorphous Hemin/Acetone-Derived Carbonized Polymer with Graphene Nanosheets for Room-Temperature NO Sensing

Jianqiang Wang, Yixun Gao, Fengjia Chen, Lulu Zhang, Hao Li, Nicolaas Frans de Rooij, Ahmad Umar, Yi-Kuen Lee, Paddy J. French, Bai Yang, Yao Wang,* and Guofu Zhou

Cite This: *ACS Appl. Mater. Interfaces* 2022, 14, 53193−53201

Read Online

ACCESS | Metrics & More | Article Recommendations | Supporting Information

ABSTRACT: Implementing parts per billion-level nitric oxide (NO) sensing at room temperature (RT) is still in extreme demand for monitoring inflammatory respiratory diseases. Herein, we have prepared a kind of core−shell structural Hemin-based nanospheres (Abbr.: Hemin-nanospheres, defined as HNSs) with the core of amorphous Hemin and the shell of acetone-derived carbonized polymer, whose core−shell structure was verified by XPS with argon-ion etching. Then, the HNS-assembled reduced graphene oxide composite (defined as HNS-rGO) was prepared for RT NO sensing. The acetone-derived carbonized polymer shell not only assists the formation of amorphous Hemin core by disrupting their crystallization to release more Fe−N_4 active sites, but provides protection to the core. Owing to the unique core−shell structure, the obtained HNS-rGO based sensor exhibited superior RT gas sensing properties toward NO, including a relatively higher response (R_a/R_g = 5.8, 20 ppm), a lower practical limit of detection (100 ppb), relatively reliable repeatability (over 6 cycles), excellent selectivity, and much higher long-term stability (less than a 5% decrease over 120 days). The sensing mechanism has also been proposed based on charge transfer theory. The superior gas sensing properties of HNS-rGO are ascribed to the more Fe−N_4 active sites available under the amorphous state of the Hemin core and to the physical protection by the shell of acetone-derived carbonized polymer. This work presents a facile strategy of constructing a high-performance carbon-based core−shell nanostructure for gas sensing.

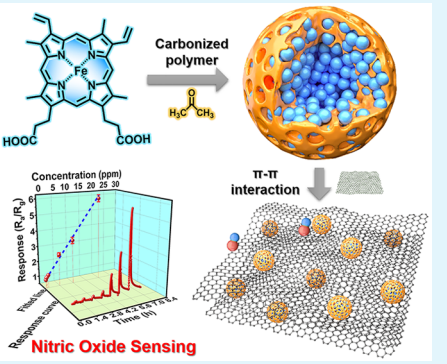

KEYWORDS: *nitric oxide sensor, Hemin, graphene, carbonized polymer, core−shell structure*

1. INTRODUCTION

Nitric oxide (NO) can diffuse across the cytomembrane freely because of its inherent lipid solubility.[1,2] This typical signaling molecule plays a critical role in transmitting physiological signals in the human body.[3] Many studies have shown that fractional exhaled nitric oxide (FeNO, parts per billion level) is a typical biomarker of respiratory inflammation, which is significantly correlated with respiratory diseases such as asthma and chronic cough.[4] Moreover, there are some recently published studies presenting the application of FeNO in the risk stratification of COVID-19 patients.[5] Hence, parts per billion-level NO monitoring showed its unique credit in the clinical diagnosis of respiratory disease. Nevertheless, the detection of parts per billion-level NO still remains a big challenge due to the instinctive short half-life and high reactivity of NO molecules.

A multitude of detection methods have been adopted to detect NO gas, such as gas chromatography−mass spectrometer (GC-MS) and Chemiluminescence,[6,7] which are sensitive to low concentrations of NO ranging from parts per trillion to parts per million. However, these methods mainly rely on bulky instruments with high-cost and complex operation, which restricted their practical applications. Hence, developing novel and facile NO sensing methods with low-cost and easy operation is urgently demanded.

In recent decades, a large amount of literature have reported metal oxide semiconductor (MOS) based chemiresistive gas sensors toward low-concentration NO.[8−10] However, most MOS-based gas sensors require relatively high operating temperatures (generally above 150 °C), because the sensing process of MOS requires the participation of oxygen species those have to be generated under high temperature.[11] High operating temperature will cause excessive energy consumption and safety concerns. The realization of room temperature

Received: September 17, 2022
Accepted: November 6, 2022
Published: November 17, 2022

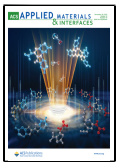

(RT) parts per billion-level NO sensing is becoming a new challenge and objective for material scientists.

Data from several studies have suggested that metal porphyrin derivatives have efficiently selective recognition of NO at RT owing to their unique heterocyclic structure and chelated metal ions,[12−14] although their poor electroconductivity would impede their applications in the realm of chemiresistive NO sensors. Graphene, as a well-known star nanomaterial, could certainly provide an ideal platform to address the above issue on account of its excellent electrical properties and functionalization capability.[15−17] In 2022, we found that assembling Hemin (Fe (III)-protoporphyrin IX) molecules onto the surface of graphene nanosheets will realize parts per billion-level NO sensing at RT with a limit of detection (LOD) of 500 ppb.[18] The Fe−N_4 active sites of Hemin molecules have the specific response to NO at RT. Unfortunately, most of the Hemin molecules will tend to form dimers via Fe−O coordination bonding and crystallize through hydrogen bonding between dimers as reported in that work.[19] The crystallization led to the occupation of Fe−N_4 active sites in crystalline Hemins, attenuating the NO sensing performances of the whole composite. According to the above inference, it can be proposed that disrupting the structure of crystalline Hemin and releasing more Fe−N_4 active sites during the synthetic process would essentially improve the sensing properties of the Hemin-based NO sensors. And the common solutions of disrupting the structure of crystalline Hemin are to break hydrogen bonds or construct three-dimensional structures.[20]

Carbonized polymer dots (CPDs), an environmentally friendly material, are usually derived from carbonization of polymer clusters under high temperature and pressure such as hydrothermal/solvothermal conditions, possessing abundant functional groups, short polymer chains and cross-linked nanostructure, simultaneously.[21] It has also been reported that acetone, which is a good solvent specially for Hemin, can be used as a carbon source to prepare acetone-derived CPDs through carbonizing under high temperature.[22,23] The as-prepared CPDs can be further carbonized to obtain continuous phase of carbonized polymer frameworks.[24] Inspired by these thoughts, aiming to disrupting the structure of crystalline Hemin and releasing more Fe−N_4 active sites during the synthetic process, the following three points could be hypothesized: (i) the abundant functional groups of acetone-derived CPDs could disrupt the hydrogen bond between Hemin dimers; (ii) the short polymer chains of acetone-derived CPDs could destroy the crystallization process of Hemin molecules; (iii) the cross-linked frameworks coming from acetone-derived CPDs could contribute to the formation of an amorphous Hemin-contained and graphene-based composite with more complex nanostructure. In a short word, this proposed assembly should show better RT NO sensing performances if the above speculations were correct.

In this work, to verify the above hypotheses, we managed an assembly of amorphous Hemin-based core−shell structural nanospheres with reduced graphene oxide nanosheets. The obtained nanocomposite (defined as HNS-rGO) were successfully prepared using a two-step fabrication procedure consisting of the synthesis of core−shell structural nanospheres with a core of amorphous Hemin and a shell of acetone-derived carbonized polymer, followed by the assembly of HNS with rGO. The morphology, structure, and chemical composition of the obtained material have systematically been characterized. As we expected, the HNS-rGO based sensor exhibited superior NO sensing performances at RT with lower practical LOD of 100 ppb, relatively higher response (R_a/R_g = 5.8, 20 ppm), relatively reliable repeatability (over 6 cycles), excellent selectivity and much higher long-term stability (less than 5% decrease over 120 days). The sensing mechanism has also been proposed based on charge transfer theory. The mechanism analysis indicated that the superior NO sensing properties should ascribe to the more Fe−N_4 active sites resulting from the amorphization of Hemin, which was caused by disturbing the hydrogen bonding between Hemin molecules with functional groups of carbonized polymers, and by simultaneously sterically blocking crystallization with their polymer chains. Meanwhile, the acetone-derived carbonized polymer shell provided the physical protection for the inner NO sensitive core as well.

2. EXPERIMENTAL SECTION

2.1. Materials. The flake graphite (325 mesh, ≥ 99.6%) was supplied by XianFeng NANO Co., Ltd. (Nanjing, P. R. China). Acetone (AR) was purchased from Guangzhou Chemical Reagent Factory (Guangzhou, P. R. China). Dialysis bag (RC, Molecular Weight Cut-Off: 1000 Da) was obtained from Shanghai green Bird Science & Technology Development Co., Ltd. (Shanghai, P. R. China). All other chemicals were purchased from Shanghai Titanchem Co., Ltd. (Shanghai, P. R. China). Ag−Pd interdigitated electrodes (IEs) were obtained from Beijing Elite Tech Co., Ltd. (Beijing, P. R. China).

2.2. Preparation of Graphene Oxide (GO). GO was synthesized by a modified Hummers' method following the procedure reported in our previous work.[18] The measured concentration of GO was 5 mg/mL.

2.3. Synthesis of HNS Nanospheres. The HNS was synthesized using a simple one-step solvothermal reaction. First, 30 mg of Hemin was dispersed in 10 mL of acetone with ultrasonication for 15 min. Then, the suspension was transferred into a 25 mL autoclave, which was followed by heating at 180 °C for 24 h. After naturally cooling to room temperature, the product was filtered by 0.22 μm membranes and further purified by water dialysis (Molecular Weight Cut-Off: 1000 Da) for 3 days. Finally, the HNS powder was obtained by lyophilization. The control groups (CG1, CG2, and CG3) were carried out employing ethyl alcohol (EtOH), N, N-dimethylformamide (DMF), and tetrahydrofuran (THF) as solvent, respectively. Similarly, the CG4 was prepared by replacing Hemin with Protoporphyrin IX.

2.4. Preparation of HNS-rGO Nanocomposite. The HNS-rGO hybrid composite was prepared via a solvothermal method. Typically, 1 mL of GO and 10 mg of HNS were orderly dispersed in 10 mL of anhydrous ethanol with ultrasonication for 10 min. Then, the mixture was heated to 80 °C for 12 h. After that, the solution was quickly transferred to a 25 mL autoclave, which was followed by heating at 120 °C for 3 h. After cooling to ambient temperature, the as-synthesized product was rinsed three times by vacuum filtration with ethanol to remove the physically adsorbed HNS. Finally, HNS-rGO dispersion was obtained after being redispersed into 10 mL of anhydrous ethanol under mild sonication. The rGO solution was obtained in the same manner without adding HNS. The control groups were carried out by replacing HNS with Hemin and CGx (x = 1, 2, 3, 4) respectively, the as-obtained samples were labeled as Hemin-rGO and CGx-rGO.

2.5. Characterization. The morphologies of the as-prepared samples were observed using a field emission scanning electron microscope (FESEM, Ultra 55, Carl Zeiss, Germany) and a transmission electron microscope (TEM, JEM-1400 PLUS, JEOL, Japan). The crystal structures of all the materials were characterized by X-ray powder diffraction (XRD; D8 Advance, Bruker, Germany), using Cu−Kα as the incident radiation. The chemical groups were determined by Fourier transform infrared spectrophotometer (FT-IR,

https://doi.org/10.1021/acsami.2c16769
ACS Appl. Mater. Interfaces 2022, 14, 53193−53201

Vertex 70, Bruker, Germany). Raman spectra were obtained by confocal Raman spectrometer (Raman, inVia, Renishaw, UK) using 532 nm laser as an excitation source. The UV−vis absorption spectra were recorded in a UV−vis spectrophotometer (UV-1900, Shimadzu, Japan). The contents of the element were analyzed by X-ray photoelectron spectroscopy (XPS; Thermo Scientific NEXSA, Thermo Fisher, USA) and argon-ion etching with a mono X-ray source Al Kα as the incident radiation. The N_2 adsorption/desorption isotherms were obtained using automatic gas adsorption analyzer (ASAP 2460, Micromeritics Instrument Corp, USA). The relative humidity was controlled by a Gas and Liquid Distribution System with Humidity Control (DGL-III, ELITE TECH. China).

2.6. Sensor Fabrication. The commercial IEs were cleaned with acetone by ultrasonication for 30 min to remove surface stains before using. First, 10 μL of sample solution was dropped onto the surface of the IEs. Then, the IEs were dried on an oven in air at 50 °C for 10 min. Finally, the gas sensors were available after cooling to ambient temperature. The typical digital camera image and SEM images of fabricated HNS-rGO sensor were shown in Figure S1.

2.7. Gas-Sensing Measurement. The resistance of the sensors was recorded by a Keithley 2450 Sourcemeter. First, the prepared IEs were placed in a chamber filled with N_2 to record the baseline. Then, after waiting for the stabilization of baseline, the IEs were transferred to a testing chamber filled with a certain concentration of target gas diluted in N_2. Finally, the IEs were transferred to a chamber filled with dry air for recovery. All the gas sensing tests were carried out at room temperature (25 ± 2 °C). For the volatile gases, including ethanol, acetone, benzene, *n*-hexane, methanol and formaldehyde, ethyl acetate, acetonitrile, and isopropanol, their vapor streams can be generated by heating the corresponding volatile compounds in a heating plate inside the chamber. In this work, the response is denoted as Response = R_a/R_g, in which R_a and R_g represent the resistance captured in N_2 and targeting gas, respectively.

3. RESULTS AND DISCUSSION

The schematic illustration of the preparation of HNS-rGO is shown in Figure 1. The HNS were fabricated by solvothermal

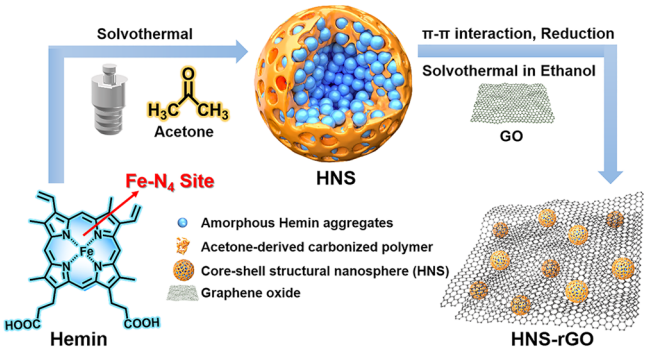

Figure 1. Synthesis process of HNS nanosphere assembled reduced graphene oxide composite HNS-rGO.

method using acetone and Hemin as raw materials. Subsequently, HNS and graphene oxide (GO) were composed via solvothermal method in ethanol, yielding a suspension of HNS-rGO.

3.1. Morphology and Structure Characterizations. The size and morphology of the synthesized HNS were characterized by scanning electron microscope (SEM) and transmission electron microscopy (TEM). The SEM image (Figure 2a) and TEM image (Figure 2b) displayed the HNS as spherical shapes with a diameter of 50 ± 10 nm. The structural details of HNS were further investigated with high-resolution TEM (HRTEM) as shown in Figure 2d. No lattice fringes were observed, indicating the HNS had an amorphous structure, which was consistent with the selected area electron diffraction (SAED) image (Figure 2c inset).

As shown in Figure S2, the high-angle annular dark-field (HAADF) TEM image, the corresponding energy-dispersive X-ray spectroscopy (EDS) spectrum, and the elemental mapping images were obtained. The mapping results displayed that the C, N, O, and Fe elements were distributed on the HNS. Moreover, the EDS spectrum revealed that HNS is composed of C, N, O, and Fe with the weight fraction of 77.15%, 6.48%, 10.01%, and 6.36%, respectively.

In addition, the N_2 adsorption/desorption isotherms (Figure S3a) was carried out to evaluate the porosity. The HNS exhibited reversible type IV physisorption behavior with a hysteresis loop. The calculated surface area of HNS was 39.7 $m^2\ g^{-1}$ using the Brunauer−Emmett−Teller (BET) model. As shown in Figure S3b, it can be seen that HNS possessed the main pore size of about 50 nm, possibly because of the random packing of HNS. Herein, what needs to be pointed out is that there existed pores of relatively small size (<4 nm), ascribing to the surface pores of HNS. In order to study the new functions endowed by solvothermal method, the UV−vis absorption spectra of HNS and raw materials Hemin were measured and shown in Figure S4. The HNS showed obvious characteristic absorption peaks (Soret peak) at 400 nm and a low-intensity band (Q-band) at 592 nm, which can be attributed to the raw materials Hemin, indicating the structure of the Hemin was not destroyed during the solvothermal process.[25,26]

Afterward, the assembly and coreduction of HNS and GO were carried out to provide the conductivity of the complex for chemiresistive sensing. As shown in Figure 2e, the gauzy graphene nanosheets and the spherical HNS were observed simultaneously in the SEM image of HNS-rGO, confirming the successful assembly of rGO and HNS, which was coincident with the TEM image of HNS-rGO (Figure 2f).

The functional groups of the prepared materials were examined by Fourier transform infrared (FT-IR) spectroscopy. As shown in Figure 3a, the vibrational peaks of GO are consistent with the presence of functional groups (C═O stretching, 1734 cm^{-1}; OH deformation, 1398 cm^{-1}; the C−OH stretching, 1226 cm^{-1}; C−O−C (epoxy group) stretching, 1080 cm^{-1}).[27,28] Compared with GO, the characteristic band of C═O stretching vibration of the carboxyl group almost disappeared in rGO, hence revealing the successful reduction.[29] In addition to the vibration bands of O−H, C═O, and C−N, the FT-IR spectrum of the HNS also exhibited one peak at 1632 cm^{-1}, which should be ascribed to the C═C stretching vibrations of the porphyrin ring.[27] As the FT-IR spectrum of HNS largely resembles that of Hemin, it could be deduced that the porphyrin rings were not eliminated during the solvothermal process, guaranteeing HNS of the ability to interact with NO specifically.[30,31] Moreover, typical peaks of both HNS and rGO appeared in the FT-IR spectra of HNS-rGO, indicating the successful assembling of HNS and rGO. The major driving force of the self-assembly should be $\pi-\pi$ interaction between conjugated structure of HNS and rGO nanosheets.[32]

To further analyze the nanostructure, we examined all the prepared materials by powder X-ray diffraction (XRD) analysis (Figure 3b). The XRD pattern of rGO exhibited a broad diffraction peak at about 23° compared to that of GO, indicating the successful reduction of GO into rGO.[33] Unlike the characteristic XRD pattern of Hemin crystals with strong and narrow diffraction peaks at 7°, 11.6°, and 24.3°, the XRD

https://doi.org/10.1021/acsami.2c16769
ACS Appl. Mater. Interfaces 2022, 14, 53193−53201

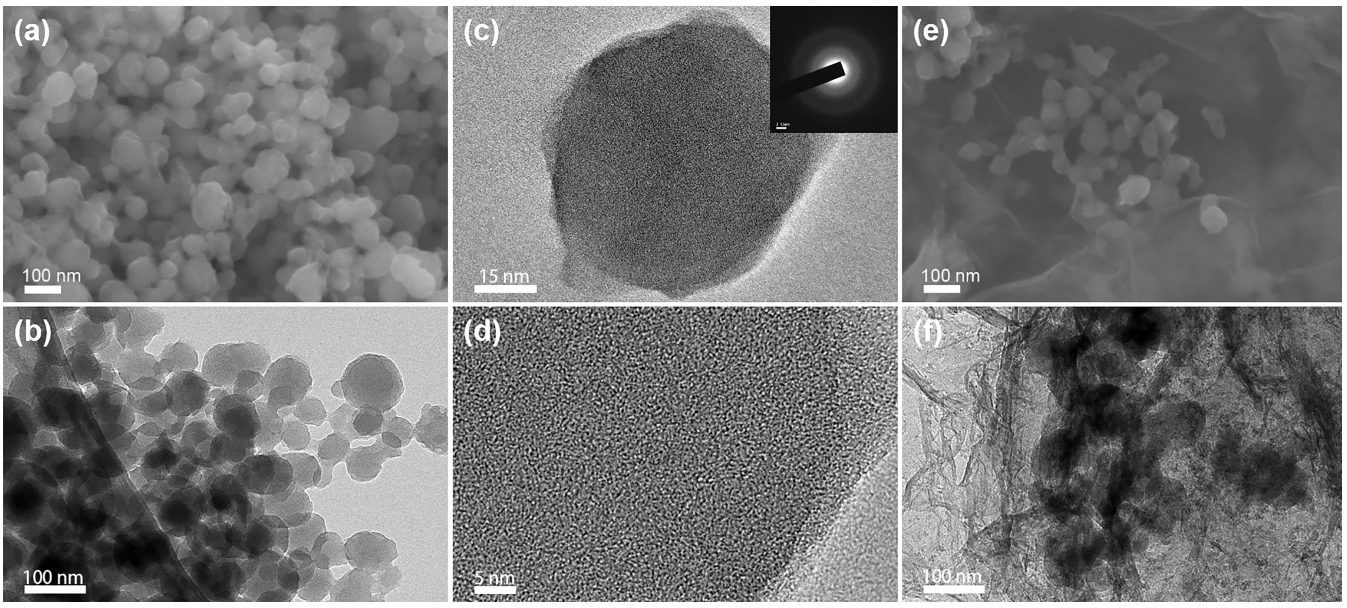

Figure 2. (a) SEM image and (b) TEM image of HNS. (c) TEM image and (d) corresponding HRTEM image of typical individual HNS. Inset: the corresponding SAED pattern. (e) SEM image and (f) TEM image of HNS-rGO.

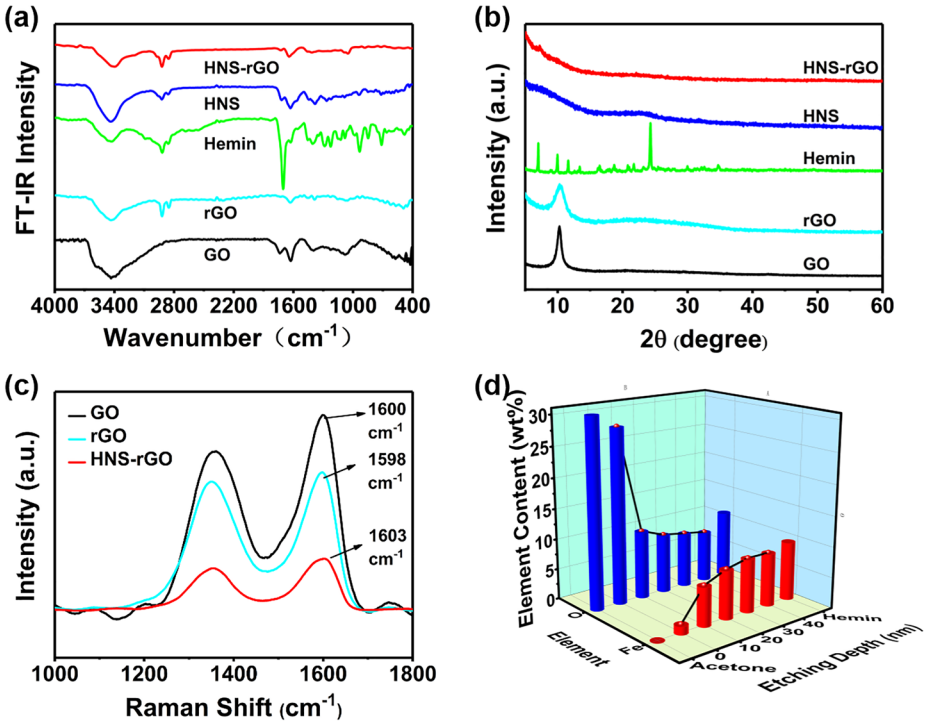

Figure 3. (a) FT-IR spectra of GO (i), rGO (ii), Hemin (iii), HNS (iv), and HNS-rGO (v). (b) Powder X-ray diffraction patterns of GO (i), rGO (ii), Hemin (iii), HNS (iv), and HNS-rGO (v). (c) Raman spectra of GO (i), rGO (ii), and HNS-rGO iii). (d) Element contents of HNS versus etching depth.

pattern of HNS revealed only one broad peak at 23°, illustrating that Hemin molecules would exist in amorphous state in HNS, possibly caused by the rearrangement of Hemin molecules under interception from acetone-derived carbonized polymer.[34,35]

The Raman spectra (Figure 3c) for GO, rGO, and HNS-rGO presented the main features of graphene-based materials. The Raman spectrum of GO showed two broad peaks at 1352 and 1600 cm^{-1}, which correspond to the D- and G-bands of graphene, respectively. After the reduction to rGO, the D- and G-band peaks became narrower and the latter shifted to 1598 cm^{-1}. The observed I_D/I_G value of rGO (0.93) was higher than that of GO (0.81), which clearly revealed the successful reduction as some functional groups of GO were eliminated during the solvothermal process.[36] The increase of the D/G intensity ratio suggested that the average size of the sp^2 domains was increased upon reduction of the GO nanosheets. In contrast, the obtained HNS-rGO showed broadened D- and G-band peaks, with the G-band peak shifted to 1603 cm^{-1}

https://doi.org/10.1021/acsami.2c16769
ACS Appl. Mater. Interfaces 2022, 14, 53193−53201

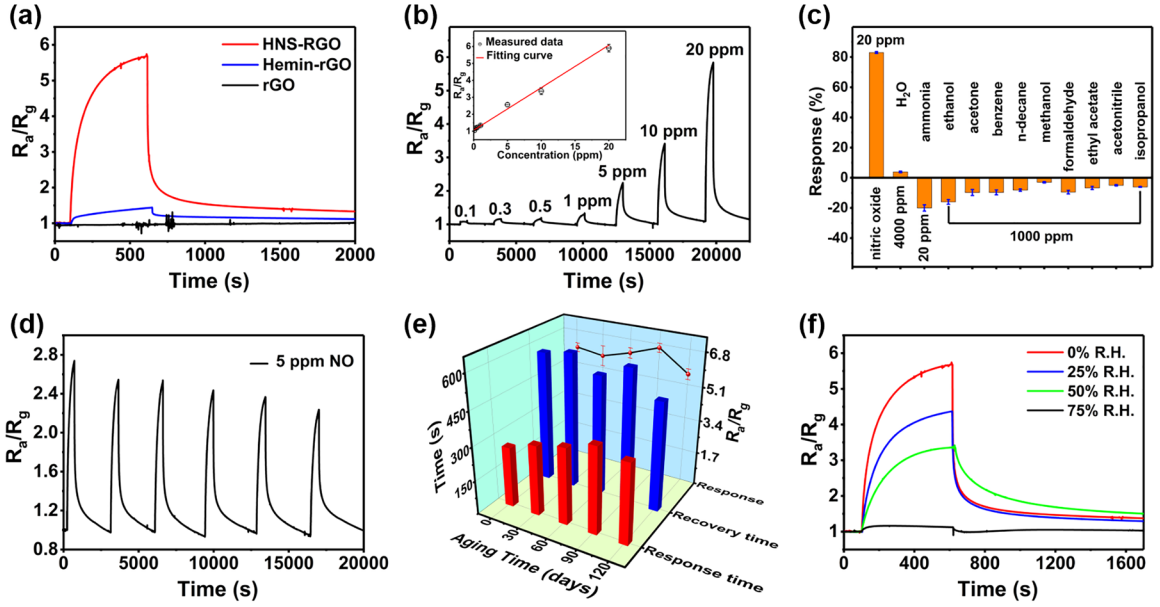

Figure 4. (a) Response curves of rGO, Hemin-rGO, and HNS-rGO sensors toward 20 ppm NO. (b) Dynamic response curve of HNS-rGO sensor to different NO concentrations ranging from 0.1 to 20 ppm. Inset: Corresponding linear fit of the responses as a function of NO concentration. (Fitting equation: $y = 0.25x + 1.06$, R-square = 0.97748.) Error bars for the data points lie within the symbols themselves. (c) selectivity of the HNS-rGO sensors toward 20 ppm NO, 4000 ppm H_2O, 20 ppm NH_3, and 1000 ppm other interferential gases, including ethanol, acetone, benzene, *n*-decane, methanol, formaldehyde, ethyl acetate, acetonitrile, and isopropanol. Error bars for the data points lie within the symbols themselves. (d) Six-cyclic response curves of the HNS-rGO sensor toward 5 ppm NO. (e) Aging test of HNS-rGO sensors toward 20 ppm NO for 120 days. (f) Response curves of HNS-rGO toward 20 ppm NO under 0−75% relative humidity.

compared to rGO, manifesting the electron transfer between rGO and HNS.[37,38]

As shown in Figure 3d, XPS with argon-ion etching was conducted to investigate the elemental composition of HNS. The core−shell structure of HNS can be confirmed from the obtained results owing to significant element content differences between the surface and interior of HNS. The detailed analysis is provided in Section 3.3.

3.2. NO Gas Sensing Properties. To investigate the gas sensing properties, we employed the as-prepared samples as sensing materials to fabricate the sensors on IEs, respectively. The details are described in Section 2.6.

The current versus voltage (I−V) curve of the HNS-rGO sensor was performed as shown in Figure S5. The excellent linearity indicated good ohmic contact between the HNS-rGO and the IEs, which could rule out the influence factors of electrodes.[39] Figure 4a demonstrated the typical gas response/recovery curves of the rGO, Hemin-rGO, and HNS-rGO toward 20 ppm NO. It is clear that HNS-rGO sensor exhibited a significantly enhanced response (R_a/R_g = 5.8) compared to rGO and Hemin-rGO. The enhanced response of HNS-rGO is mainly attributed to the specific core−shell structure of HNS, which will be discussed in section 3.3. As shown in Figure S6, the HNS-rGO displayed relatively rapid response and recovery toward 20 ppm NO with a T_{res} of 261 s and a T_{rec} of 585 s, respectively. Figure 4b exhibited the successive dynamic-sensing response of the HNS-rGO sensor toward 0.1−20 ppm NO with the corresponding response (R_a/R_g) from 1.08 to 5.8. The response values showed good linearity to NO concentration, which is of significance for practical applications (Figure 4b inset).

The selectivity of the HNS-rGO sensor was explored as shown in Figure 4c. To facilitate the comparison, here the response is converted as Response $= \frac{\Delta R}{R_a} = \frac{R_a - R_g}{R_a}100\%$. The response ($\Delta R/R_a$ = 82.7%) of HNS-rGO sensor toward 20 ppm NO was much higher than other exhaled gases including 4000 ppm H_2O, 20 ppm NH_3, and 1000 ppm ethanol, acetone, benzene, *n*-hexane, methanol formaldehyde, ethyl acetate, acetonitrile, and isopropanol. Benefiting from the specific interaction between HNS and NO molecules, the HNS-rGO sensors performed extremely sensitive to NO even in the presence of other exhaled interfering gases (Figure S7), which is exactly demanded for practical application in clinical diagnosis as we discussed before.

The repeatability and stability are also vital criteria for gas sensors. As shown in Figure 4d, the six successively cyclical response-recovery curves of HNS-rGO toward 5 ppm NO were obtained. Average response of 2.57 with a relatively small standard deviation of 10% was obtained, indicating the relatively reliable repeatability of HNS-rGO sensor. Moreover, a monthly aging test was carried out for four months (Figure 4e). The sensor revealed highly stable response (less than 5% decrease) and relatively short response/recovery time (261−381 s/481−601 s) toward 20 ppm NO over the whole period time. To investigate the humidity effect on the gas sensing performance, we exposed the HNS-rGO sensors to different relative humidity (RH) from 0% to 75% and the corresponding gas sensing response toward 20 ppm NO was recorded (Figure 4f). The gas sensing responses of HNS-rGO would be suppressed along with the increase of RH, indicating the sensor is not resistant to humidity, this question could be addressed by the technology of drying the import gases in advance, similar to what has been developed in the modern exhaled breath detection.[40] Although the sensing properties of HNS-rGO was inhibited under high RH, it could rapidly recover once switching to low RH, indicating that the HNS-rGO composite was still stable under high humidity (Figure S8). Previously reported works about carbon-based NO gas

https://doi.org/10.1021/acsami.2c16769
ACS Appl. Mater. Interfaces 2022, 14, 53193−53201

Table 1. Summary of the NO Gas Sensing Performance of Carbon-Based Materials at Room Temperature[a]

materials	NO (ppm)	response	T_{res}/T_{rec}(s/s)	D_R (ppm)	stability (days)	pLOD (ppm)
TiO_2@NGQDs[b][41]	100	0.76	235/285	10−100		10
MoS_2/rGO/paper[42]	2	1.06	150/>600	2−10		2
CNFs/CoS_2/MoS_2[43]	10	∼1.045	1200/6000	1−100		1
SWNT@MoS_2[44]	100	1.18	45/528	1−300		1
TiO_2/rGO[45]	2.75	1.06	440/881	0.69−2.75		0.69
N-rGO[46]	1	0.59	∼100/--	0.4−1	7	0.4
SWCNT@PEI[47]	1	∼2.5	∼1800/>3000	0.1−5		0.1
en-APTAS@SWCNTs[48]	0.1	1.25	∼600/>600		35	0.1
WS_2/MWCNT[49]	0.01	∼1.1	285/198	0.001−0.1	42	0.001
Hemin-N-rGO[18]	20	3	400/1000	0.5−20	30	0.5
	1	1.34	229/770			
HNS-rGO (this work)	20	5.8	261/585	0.1−20	120	0.1
	0.1	1.08	80/381			

[a]Response time (T_{res}), recovery time (T_{rec}), practical limit of detection (pLOD), studied detection range (D_R). Stability refers to the long-term stability. The response is denoted as Response = R_a/R_g. [b]The gas sensing performance of TiO_2@NGQDs were carried out under 365 nm illumination.

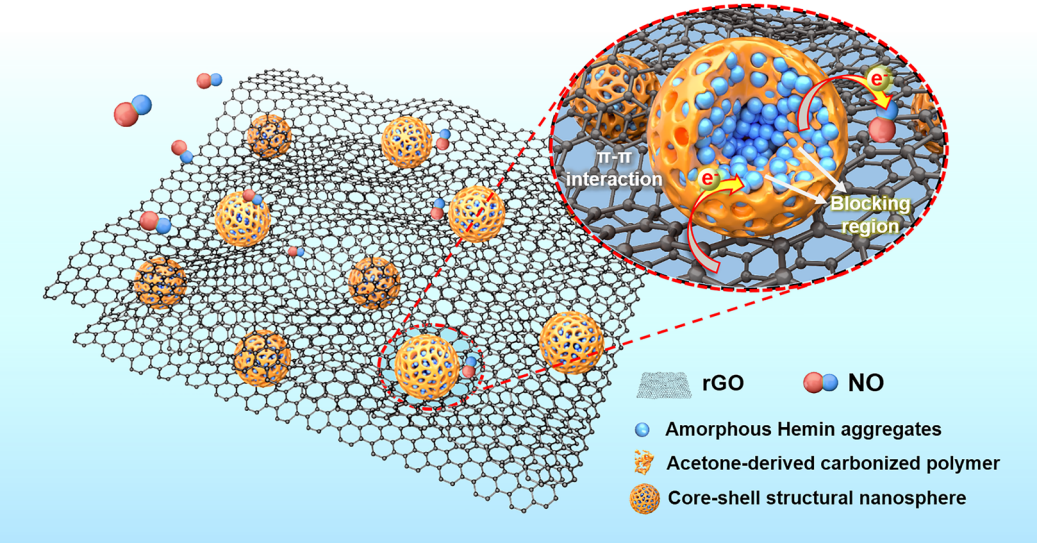

Figure 5. Schematic diagram of the sensing mechanism of the HNS-rGO toward NO.

sensors at RT were summarized in Table 1. The gas sensing performances of the HNS-rGO could fairly rival those of listed NO gas sensors. Moreover, the HNS-rGO based sensors have a practical LOD with 100 ppb, which is a quite low practical LOD toward NO at RT for carbon-based sensing materials. Meanwhile, the HNS-rGO based sensor exhibits a relatively short response/recovery time and excellent long-term stability. The outstanding NO sensing properties of HNS-rGO could therefore make it a promising candidate for RT NO sensors.

3.3. Gas Sensing Mechanism. Based on the previous description, it could be speculated that HNS would have a core−shell structure composed of a core of amorphous hemin and acetone-derived shell surrounded. To verify this deduction, we conducted XPS with argon-ion etching.

As shown in Figure 3d and Table S1, before etching, the oxygen and iron contents on the original surface of HNS were 28.45% and 1.32%, respectively, which is similar to the intrinsic element proportion of acetone. Surprisingly, as the etch depth increased to 10, 20, 30, 40, and 50 nm, the oxygen content descended to 11.04, 9.56, 8.93, and 8.29%. On the contrary, the iron content rose to 6.33, 7.88, 8.67, and 8.61%. From this result, it could be deduced that HNS possessed a typical characteristic of core−shell structure.[50] The acetone moieties on the outer surface of HNS serve as the main shell structure containing more oxygen elements but no iron elements, whereas the interior of HNS composed of Hemin-derived spheres with fewer oxygen elements but more iron elements. Moreover, the results of XPS indicated that the core and shell sections of HNS had blurry boundaries among each other. The existence of acetone-derived carbonized polymer did influence the assembly process of Hemin and played a critical role in its rearrangement from crystalline to amorphous state. Combined with our previous work,[18] the sensing mechanism based on charge transfer has been proposed as below.

It is apparent that NO would act as an oxidizer in the gas sensing process of the HNS-rGO sensor based on the comparison with the typical reductive gas ammonia (Figure 4c). In general, rGO exhibited p-type semiconducting behavior whose resistance will reduce along with the increase of hole concentration.[16,18] As shown in Figure 5, NO molecules absorbed onto the surface of HNS could contact with the Fe^{3+} ion of the Fe−N_4 moiety through the hole of the acetone layer.

https://doi.org/10.1021/acsami.2c16769
ACS Appl. Mater. Interfaces 2022, 14, 53193−53201

Afterward, electrons are transferred from graphene to Fe^{3+}, and subsequently given to the NO molecules benefiting from the strong electronegativity of NO. Hence, the hole concentration of rGO would increase with the addition of NO, which induces the decline of the resistance of the sensing material. On the one hand, the acetone-derived carbonized polymer could induce the formation of the amorphous Hemin core to absorb more NO molecules than crystalline Hemin. On the other hand, it provides physical protection to the Hemin core, resulting in high long-term stability of HNS. After assembling with conductive rGO through $\pi-\pi$ interaction, these unique core−shell structural nanospheres would interact with NO efficiently and selectively, which could be revealed as electrical response via the electron transport between HNS and rGO.

To further investigate the formation mechanism of the core−shell structural HNS, control groups were carried out by replacing acetone with ethyl alcohol (EtOH), N, N-dimethylformamide (DMF) and tetrahydrofuran (THF), and the corresponding products were named as CG1, CG2 and CG3, respectively. From their TEM images (Figure S9a, b, c), obvious carbon dots were observed in all the samples, which was caused by the high carbonization of Hemin without the protection of acetone moieties. Similarly, control group (CG4) of replacing Hemin with Protoporphyrin IX was conducted with the only difference that no Fe^{3+} exists in the porphyrin ring. As shown in Figure S9d, gauze-like lamellar materials instead of spheres were observed, possibly because the Fe^{3+} provided essential driving force for the formation of amorphous Hemin which could assemble into the core by coordination interaction.[51] As displayed in Figure S10, all the four control samples toward 20 ppm NO at RT exhibited significantly weakened response values compared to the HNS-rGO sensor. Therefore, it could be concluded that the core−shell structure of HNS is dominant to the sensing properties of the obtained sensor.

4. CONCLUSION

In summary, the amorphous Hemin core−shell structural HNS nanospheres were successfully synthesized by a simple solvothermal method. The core−shell structure was confirmed by XPS with argon-ion etching. The sensors based on HNS-rGO showed excellent gas sensing performance toward NO at RT, with a high response (R_a/R_g = 5.8, 20 ppm), relatively reliable repeatability, remarkable selectivity, superior sensing linearity and long-term stability. More significantly, the sensor showed a quite low practical LOD of 100 ppb toward NO at RT, while having relatively short response/recovery time. Moreover, it was explored that the outstanding NO gas sensing performance was mainly attributed to the more $Fe-N_4$ active sites resulting from amorphous Hemin core, and to the physical protection by the shell of acetone-derived carbonized polymer. This work not only presents a new strategy for devising high-performance NO sensing systems, but develops an avenue for preparation of carbonized polymer-contained core−shell structural materials.

■ ASSOCIATED CONTENT

Supporting Information

The Supporting Information is available free of charge at https://pubs.acs.org/doi/10.1021/acsami.2c16769.

Digital image and SEM images of fabricated HNS-rGO sensor, HAADF TEM image of HNS, corresponding EDS elemental mapping and EDS spectrum, N_2 adsorption/desorption isotherms and pore-size distribution analysis of HNS, UV−vis absorption spectra of Hemin and HNS, I−V characteristics of HNS-rGO sensor, T_{res} and T_{rec} measurement of HNS-rGO sensor, the competitive gas sensing experiments, Humidity resistance test of humidity in situ switching, TEM images of control groups, gas sensing response curves of control groups, and the results of XPS with argon-ion etching (PDF)

■ AUTHOR INFORMATION

Corresponding Author

Yao Wang − *Guangdong Provincial Key Laboratory of Optical Information Materials and Technology, Institute of Electronic Paper Displays, South China Academy of Advanced Optoelectronics and National Center for International Research on Green Optoelectronics, South China Normal University, Guangzhou 510006, P. R. China;* orcid.org/0000-0002-0713-5018; Email: wangyao@m.scnu.edu.cn

Authors

Jianqiang Wang − *Guangdong Provincial Key Laboratory of Optical Information Materials and Technology, Institute of Electronic Paper Displays, South China Academy of Advanced Optoelectronics and National Center for International Research on Green Optoelectronics, South China Normal University, Guangzhou 510006, P. R. China*

Yixun Gao − *Guangdong Provincial Key Laboratory of Optical Information Materials and Technology, Institute of Electronic Paper Displays, South China Academy of Advanced Optoelectronics and National Center for International Research on Green Optoelectronics, South China Normal University, Guangzhou 510006, P. R. China;* orcid.org/0000-0001-8617-472X

Fengjia Chen − *Division of Pulmonary and Critical Care Medicine, The First Affiliated Hospital of Sun Yat-sen University, Guangzhou 510006, P. R. China; Institute of Pulmonary Diseases, Sun Yat-sen University, Guangzhou 510006, P. R. China*

Lulu Zhang − *Guangdong Provincial Key Laboratory of Optical Information Materials and Technology, Institute of Electronic Paper Displays, South China Academy of Advanced Optoelectronics and National Center for International Research on Green Optoelectronics, South China Normal University, Guangzhou 510006, P. R. China*

Hao Li − *Guangdong Provincial Key Laboratory of Optical Information Materials and Technology, Institute of Electronic Paper Displays, South China Academy of Advanced Optoelectronics and National Center for International Research on Green Optoelectronics, South China Normal University, Guangzhou 510006, P. R. China*

Nicolaas Frans de Rooij − *National Center for International Research on Green Optoelectronics, South China Normal University, Guangzhou 510006, P. R. China*

Ahmad Umar − *Promising Centre for Sensors and Electronic Devices, Department of Chemistry, Faculty of Science and Arts, Najran University, Najran 11001, Kingdom of Saudi Arabia*

Yi-Kuen Lee − *Department of Mechanical & Aerospace Engineering and Department of Electronic & Computer Engineering, Hong Kong University of Science and*

https://doi.org/10.1021/acsami.2c16769
ACS Appl. Mater. Interfaces 2022, 14, 53193−53201

Technology, Kowloon, Hong Kong Special Administrative Region

Paddy J. French − *BE Laboratory, EWI, Delft University of Technology, Delft 2628CD, The Netherland*

Bai Yang − *State Key Lab of Supramolecular Structure and Materials College of Chemistry, Jilin University, Changchun 130012, P. R. China;* orcid.org/0000-0002-3873-075X

Guofu Zhou − *Guangdong Provincial Key Laboratory of Optical Information Materials and Technology, Institute of Electronic Paper Displays, South China Academy of Advanced Optoelectronics and National Center for International Research on Green Optoelectronics, South China Normal University, Guangzhou 510006, P. R. China;* orcid.org/0000-0003-1101-1947

Complete contact information is available at: https://pubs.acs.org/10.1021/acsami.2c16769

Notes

The authors declare no competing financial interest.

■ ACKNOWLEDGMENTS

This work was supported by the National Natural Science Foundation of China (Grants 51973070 and 51773069), Science and Technology Program of Guangzhou (2019050001), Innovative Team Project of Education Bureau of Guangdong Province, Guangdong Science and Technology Project-International Cooperation, Guangdong Basic and Applied Basic Research Foundation (2021A1515012420), Startup Foundation from SCNU, Guangdong Provincial Key Laboratory of Optical Information Materials and Technology (2017B030301007), MOE International Laboratory for Optical Information Technologies, and the 111 Project.

■ REFERENCES

(1) Subczynski, W. K.; Lomnicka, M.; Hyde, J. S. Permeability of Nitric Oxide through Lipid Bilayer Membranes. *Free Radical Res.* **1996**, *24* (5), 343−349.

(2) Möller, M. N.; Denicola, A. Diffusion of Nitric Oxide and Oxygen in Lipoproteins and Membranes Studied by Pyrene Fluorescence Quenching. *Free Radical Bio. Med.* **2018**, *128*, 137−143.

(3) Calabrese, V.; Mancuso, C.; Calvani, M.; Rizzarelli, E.; Butterfield, D. A.; Giuffrida Stella, A. M. Nitric Oxide in the Central Nervous System: Neuroprotection versus Neurotoxicity. *Nat. Rev. Neurosci.* **2007**, *8* (10), 766−775.

(4) Gustafsson, L. E.; Leone, A. M.; Persson, M. G.; Wiklund, N. P.; Moncada, S. Endogenous Nitric Oxide is Present in the Exhaled Air of Rabbits, Guinea Pigs and Humans. *Biochem. Bioph. Res. Co.* **1991**, *181* (2), 852−857.

(5) Banga, I.; Paul, A.; France, K.; Micklich, B.; Cardwell, B.; Micklich, C.; Prasad, S. E.Co.Tech-Electrochemical Handheld Breathalyzer COVID Sensing Technology. *Sci. Rep.* **2022**, *12* (1), 1−11.

(6) Kipping, P. J.; Jeffery, P. G. Detection of Nitric Oxide by Gas-chromatography. *Nature* **1963**, *200* (4913), 1314−1314.

(7) Bates, J. N. Nitric Oxide Measurement by Chemiluminescence Detection. *Neuroprotocols* **1992**, *1* (2), 141−149.

(8) Naderi, H.; Hajati, S.; Ghaedi, M.; Espinos, J. P. Highly Selective Few-ppm NO Gas-sensing Based on Necklace-like Nanofibers of ZnO/CdO n-n type I Heterojunction. *Sens. Actuators, B* **2019**, *297*, 126774.

(9) Li, C.; Song, B.-Y.; Lv, M.-S.; Chen, G.-L.; Zhang, X.-F.; Deng, Z.-P.; Xu, Y.-M.; Huo, L.-H.; Gao, S. Highly Sensitive and Selective Nitric Oxide Sensor Based on Biomorphic ZnO Microtubes with Dual-defects Assistance at Low Temperature. *Chem. Eng. J.* **2022**, *446*, 136846.

(10) Song, B.-Y.; Li, C.; Zhang, X.-F.; Gao, R.; Cheng, X.-L.; Deng, Z.-P.; Xu, Y.-M.; Huo, L.-H.; Gao, S. A Highly Sensitive and Selective Nitric Oxide/Butanone Temperature-Dependent Sensor Based on Waste Biomass-Derived Mesoporous SnO_2 Hierarchical Microtubes. *J. Mater. Chem. A* **2022**, *10* (27), 14411−14422.

(11) Lontio Fomekong, R.; Saruhan, B.; Debliquy, M.; Lahem, D. High-Temperature NO Sensing Performance of WO_3 Deposited by Spray Coating. *RSC Adv.* **2022**, *12* (34), 22064−22069.

(12) Nguyen, T. Q.; Escaño, M. C. S.; Kasai, H. Nitric Oxide Adsorption Effects on Metal Phthalocyanines. *J. Phys. Chem. B* **2010**, *114* (31), 10017−10021.

(13) Nyokong, T.; Vilakazi, S. Phthalocyanines and Related Complexes as Electrocatalysts for the Detection of Nitric Oxide. *Talanta* **2003**, *61* (1), 27−35.

(14) Sarkar, A.; Carter, E. L.; Harland, J. B.; Speelman, A. L.; Lehnert, N.; Ragsdale, S. W. Ferric Heme as a CO/NO Sensor in the Nuclear Receptor Rev-Erbβ by Coupling Gas Binding to Electron Transfer. *Proc. Natl. Acad. Sci. U. S. A.* **2021**, *118* (3), e2016717118.

(15) Qiu, J.; Hu, X.; Min, X.; Quan, W.; Tian, R.; Ji, P.; Zheng, H.; Qin, W.; Wang, H.; Pan, T.; Cheng, S.; Chen, X.; Zhang, W.; Wang, X. Observation of Switchable Dual-Conductive Channels and Related Nitric Oxide Gas-Sensing Properties in the N-rGO/ZnO Heterogeneous Structure. *ACS Appl. Mater. Interfaces* **2020**, *12* (17), 19755−19767.

(16) Hu, H.; Liang, H.; Fan, J.; Guo, L.; Li, H.; de Rooij, N. F.; Umar, A.; Algarni, H.; Wang, Y.; Zhou, G. Assembling Hollow Cactus-Like ZnO Nanorods with Dipole-Modified Graphene Nanosheets for Practical Room-Temperature Formaldehyde Sensing. *ACS Appl. Mater. Interfaces* **2022**, *14* (11), 13186−13195.

(17) Ogbeide, O.; Bae, G.; Yu, W.; Morrin, E.; Song, Y.; Song, W.; Li, Y.; Su, B.-L.; An, K.-S.; Hasan, T. Inkjet-Printed rGO/binary Metal Oxide Sensor for Predictive Gas Sensing in a Mixed Environment. *Adv. Funct. Mater.* **2022**, *32* (25), 2113348.

(18) Gao, Y.; Wang, J.; Feng, Y.; Cao, N.; Li, H.; Rooij, N. F.; Umar, A.; French, P. J.; Wang, Y.; Zhou, G. Carbon-Iron Electron Transport Channels in Porphyrin−Graphene Complex for ppb-Level Room Temperature NO Gas Sensing. *Small* **2022**, *18* (11), 2103259.

(19) Pagola, S.; Stephens, P. W.; Bohle, D. S.; Kosar, A. D.; Madsen, S. K. The Structure of Malaria Pigment β-Haematin. *Nature* **2000**, *404* (6775), 307−310.

(20) Xing, R.; Zou, Q.; Yuan, C.; Zhao, L.; Chang, R.; Yan, X. Self-Assembling Endogenous Biliverdin as a Versatile Near-Infrared Photothermal Nanoagent for Cancer Theranostics. *Adv. Mater.* **2019**, *31* (16), 1900822.

(21) Xia, C.; Zhu, S.; Feng, T.; Yang, M.; Yang, B. Evolution and Synthesis of Carbon Dots: From Carbon Dots to Carbonized Polymer Dots. *Adv. Sci.* **2019**, *6* (23), 1901316.

(22) Hou, H.; Banks, C. E.; Jing, M.; Zhang, Y.; Ji, X. Carbon Quantum Dots and Their Derivative 3D Porous Carbon Frameworks for Sodium-Ion Batteries with Ultralong Cycle Life. *Adv. Mater.* **2015**, *27* (47), 7861−7866.

(23) Wang, Q.; Gao, Y.; Wang, B.; Guo, Y.; Ahmad, U.; Wang, Y.; Wang, Y.; Lu, S.; Li, H.; Zhou, G. S,N-Codoped Oil-Soluble Fluorescent Carbon Dots for a High Color-Rendering WLED. *J. Mater. Chem. C* **2020**, *8* (13), 4343−4349.

(24) Chen, X.; Gao, H.; Yang, M.; Dong, W.; Huang, X.; Li, A.; Dong, C.; Wang, G. Highly Graphitized 3D Network Carbon for Shape-Stabilized Composite PCMs with Superior Thermal Energy Harvesting. *Nano Energy* **2018**, *49*, 86−94.

(25) Qu, R.; Shen, L.; Chai, Z.; Jing, C.; Zhang, Y.; An, Y.; Shi, L. Hemin-Block Copolymer Micelle as an Artificial Peroxidase and Its Applications in Chromogenic Detection and Biocatalysis. *ACS Appl. Mater. Interfaces* **2014**, *6* (21), 19207−19216.

(26) Ryabova, E. S.; Dikiy, A.; Hesslein, A. E.; Bjerrum, M. J.; Ciurli, S.; Nordlander, E. Preparation and Reactivity Studies of Synthetic Microperoxidases Containing b-Type Heme. *J. Biol. Inorg. Chem.* **2004**, *9* (4), 385−395.

(27) Jahan, M.; Bao, Q.; Loh, K. P. Electrocatalytically Active Graphene-Porphyrin MOF Composite for Oxygen Reduction Reaction. *J. Am. Chem. Soc.* **2012**, *134* (15), 6707−6713.
(28) Xu, Y.; Bai, H.; Lu, G.; Li, C.; Shi, G. Flexible Graphene Films via the Filtration of Water-Soluble Noncovalent Functionalized Graphene Sheets. *J. Am. Chem. Soc.* **2008**, *130* (18), 5856−5857.
(29) Chen, Z.; Wang, J.; Pan, D.; Wang, Y.; Noetzel, R.; Li, H.; Xie, P.; Pei, W.; Umar, A.; Jiang, L.; Li, N.; Rooij, N. F. d.; Zhou, G. Mimicking a Dog's Nose: Scrolling Graphene Nanosheets. *ACS Nano* **2018**, *12* (3), 2521−2530.
(30) Hu, F. X.; Xie, X.; Wang, D.; Yang, H. B.; Gu, Y.; Chen, B.; Zhang, C.; Rao, Q.; Li, Q.; Guo, C. Three-Dimensional Cell-Adhesive Matrix of Silk Cocoon Derived Carbon Fiber Assembled with Iron-Porphyrin for Monitoring Cell Released Signal Molecules. *Sens. Actuators, B* **2021**, *334*, 129594.
(31) Hao, X.; Hu, F.; Gu, Y.; Yang, H.; Li, C.; Guo, C. Molecularly Assembled Graphdiyne with Atomic Sites for Ultrafast and Real-Time Detection of Nitric Oxide in Cell Assays. *Biosens. Bioelectron.* **2022**, *195*, 113630.
(32) Unnikrishnan, B.; Wu, C.-W.; Chen, I. W. P.; Chang, H.-T.; Lin, C.-H.; Huang, C.-C. Carbon Dot-Mediated Synthesis of Manganese Oxide Decorated Graphene Nanosheets for Supercapacitor Application. *ACS Sustain. Chem. Eng.* **2016**, *4* (6), 3008−3016.
(33) Mao, S.; Pu, H.; Chen, J. Graphene Oxide and its Reduction: Modeling and Experimental Progress. *RSC Adv.* **2012**, *2* (7), 2643−2662.
(34) Xie, Y.; Tang, C.; Hao, Z.; Lv, Y.; Yang, R.; Wei, X.; Deng, W.; Wang, A.; Yi, B.; Song, Y. Carbonization of Self-Assembled Nanoporous Hemin with a Significantly Enhanced Activity for the Oxygen Reduction Reaction. *Faraday Discuss.* **2014**, *176* (0), 393−408.
(35) Olafson, K. N.; Rimer, J. D.; Vekilov, P. G. Growth of Large Hematin Crystals in Biomimetic Solutions. *Cryst. Growth Des.* **2014**, *14* (5), 2123−2127.
(36) Liang, H.; Guo, L.; Cao, N.; Hu, H.; Li, H.; Frans de Rooij, N.; Umar, A.; Algarni, H.; Wang, Y.; Zhou, G. Practical Room Temperature Formaldehyde Sensing Based on a Combination of Visible-Light Activation and Dipole Modification. *J. Mater. Chem. A* **2021**, *9* (42), 23955−23967.
(37) Wang, T.; Bi, X.; Wang, L.; Liu, M.; Yu, W. W.; Zhu, Z.; Sui, N. Biomimetic Design of Graphdiyne Supported Hemin for Enhanced Peroxidase-Like Activity. *J. Colloid Interface Sci.* **2022**, *607*, 470−478.
(38) Geng, J.; Jung, H.-T. Porphyrin Functionalized Graphene Sheets in Aqueous Suspensions: From the Preparation of Graphene Sheets to Highly Conductive Graphene Films. *J. Phys. Chem. C* **2010**, *114* (18), 8227−8234.
(39) Fowler, J. D.; Allen, M. J.; Tung, V. C.; Yang, Y.; Kaner, R. B.; Weiller, B. H. Practical Chemical Sensors from Chemically Derived Graphene. *ACS Nano* **2009**, *3* (2), 301−306.
(40) Silkoff, P. E.; Carlson, M.; Bourke, T.; Katial, R.; Ögren, E.; Szefler, S. J. The Aerocrine Exhaled Nitric Oxide Monitoring System NIOX is Cleared by the US Food and Drug Administration for Monitoring Therapy in Asthma. *J. Allergy Clin. Immun.* **2004**, *114* (5), 1241−1256.
(41) Murali, G.; Reddeppa, M.; Seshendra Reddy, C.; Park, S.; Chandrakalavathi, T.; Kim, M.-D.; In, I. Enhancing the Charge Carrier Separation and Transport via Nitrogen-Doped Graphene Quantum Dot-TiO_2 Nanoplate Hybrid Structure for an Efficient NO Gas Sensor. *ACS Appl. Mater. Interfaces* **2020**, *12* (11), 13428−13436.
(42) Duy, L. T.; Noh, Y. G.; Seo, H. Improving Graphene Gas Sensors via a Synergistic Effect of Top Nanocatalysts and Bottom Cellulose Assembled Using a Modified Filtration Technique. *Sens. Actuators, B* **2021**, *334*, 129676.
(43) Hou, S.; Pang, R.; Chang, S.; Ye, L.; Xu, J.; Wang, X.; Zhang, Y.; Shang, Y.; Cao, A. Synergistic CNFs/CoS_2/MoS_2 Flexible Films with Unprecedented Selectivity for NO Gas at Room Temperature. *ACS Appl. Mater. Interfaces* **2020**, *12* (26), 29778−29786.
(44) Li, Y.; Pang, R.; Meng, W.; Zhang, D.; Li, M.; Xia, Z.; Feng, J.; Li, H.; Cao, A.; Shang, Y. Space-Confined Synthesis of SWNT Bundles Wrapped by MoS_2 Crystalline Layers as Flexible Sensors and Detectors. *Carbon* **2022**, *195*, 19−26.
(45) Kuchi, C.; Naresh, B.; Reddy, P. S. In Situ TiO_2-rGO Nanocomposite for Low Concentration NO Gas Sensor. *ECS J. Solid State Sc.* **2021**, *10* (3), 037008.
(46) Chang, Y.-S.; Chen, F.-K.; Tsai, D.-C.; Kuo, B.-H.; Shieu, F.-S. N-Doped Reduced Graphene Oxide for Room-Temperature NO Gas Sensors. *Sci. Rep.* **2021**, *11* (1), 20719.
(47) Jeon, J.-Y.; Kang, B.-C.; Byun, Y. T.; Ha, T.-J. High-Performance Gas Sensors Based on Single-Wall Carbon Nanotube Random Networks for the Detection of Nitric Oxide Down to the ppb-Level. *Nanoscale* **2019**, *11* (4), 1587−1594.
(48) Lim, N.; Kim, K. H.; Byun, Y. T. Preparation of Defected SWCNTs Decorated with en-APTAS for Application in High-Performance Nitric Oxide Gas Detection. *Nanoscale* **2021**, *13* (13), 6538−6544.
(49) Singh, S.; Saggu, I. S.; Chen, K.; Xuan, Z.; Swihart, M. T.; Sharma, S. Humidity-Tolerant Room-Temperature Selective Dual Sensing and Discrimination of NH_3 and NO Using a WS_2/MWCNT Composite. *ACS Appl. Mater. Interfaces* **2022**, *14* (35), 40382−40395.
(50) Zhang, T.; Zhao, F.; Li, L.; Qi, B.; Zhu, D.; Lü, J.; Lü, C. Tricolor White-Light-Emitting Carbon Dots with Multiple-Cores@Shell Structure for WLED Application. *ACS Appl. Mater. Interfaces* **2018**, *10* (23), 19796−19805.
(51) Chen, J.; Chen, F.; Zhang, L.; Yang, Z.; Deng, T.; Zhao, Y.; Zheng, T.; Gan, X.; Zhong, H.; Geng, Y.; Fu, X.; Wang, Y.; Yu, C. Self-Assembling Porphyrins as a Single Therapeutic Agent for Synergistic Cancer Therapy: A One Stone Three Birds Strategy. *ACS Appl. Mater. Interfaces* **2021**, *13* (24), 27856−27867.

https://doi.org/10.1021/acsami.2c16769
ACS Appl. Mater. Interfaces 2022, 14, 53193−53201